Viscous dissipation effects on hybrid nanofluid flow over a non-linearly shrinking sheet with power-law velocity

Iskandar Waini [a,*], Sumayyah Alabdulhady [b], Anuar Ishak [c], Ioan Pop [d]

[a] *Fakulti Teknologi dan Kejuruteraan Industri dan Pembuatan, Universiti Teknikal Malaysia Melaka, Hang Tuah Jaya, 76100, Durian Tunggal, Melaka, Malaysia*
[b] *Department of Mathematics, Faculty of Science, Qassim University, Qassim, 52571, Saudi Arabia*
[c] *Department of Mathematical Sciences, Faculty of Science and Technology, Universiti Kebangsaan Malaysia, 43600, UKM Bangi, Selangor, Malaysia*
[d] *Department of Mathematics, Babeş-Bolyai University, 400084, Cluj-Napoca, Romania*

ARTICLE INFO

ABSTRACT

This research intends to investigate the effect of the nonlinearity of the surface velocity on the hybrid nanofluid flow behavior. Here, the total composition of Al_2O_3 (alumina) as well as Cu (copper) volume fractions, are implemented in a one-to-one ratio and then dispersed in water. The similarity equations are gained employing a similarity transformation, which is programmed in MATLAB software. The dual solutions are attainable for certain ranges with respect to the mass flux parameter S and the power-law index n. Also, the turning point occurs in the region of $S < 0$ and $n > 1$. Besides, the rise of n led to reduce the skin friction as well as the heat transfer co-efficients with 39.44 % and 11.71 % reduction, respectively. Moreover, 14.39 % reduction of the heat transfer rate is observed in the presence of viscous dissipation (Eckert number). It is found that only the first solution is stable as time progresses. Generally, this study gives scientists and engineers a starting point for predicting how to control the parameters to achieve the best results for relevant practical applications.

1. Introduction

The boundary layer flow induced by a shrinking or stretching surface possesses many practical applications in manufacturing and industrial processes, e.g. wire drawing, metal or polymer extrusions as well as continuous glass casting. Here, Crane [1] was the earliest to examine the flow over a linearly stretching surface. Different from the stretching case, the flow induced by a shrinking surface has only become intriguing among researchers quite recently. This type of reverse flow is such kind pondered by Goldstein [2]. Wang [3] discovered that an outside force is required to confine the flow within the boundary layer. This can be done by adding an external flow or by introducing suction at the boundary, see also Miklavčič and Wang [3]. Additionally, the nonlinearly stretching or shrinking sheet was considered by several researchers, for example, Vajravelu [4], Cortell [5,6], Ishak et al. [7,8], and Rohni et al. [9].

Nanofluid resembles a new type of fluid comprising stable colloidal dispersion of nanometer-sized particles, metallic or non-metallic, in a base fluid such as water, organic liquids, polymeric solutions or other general liquids. This fluid has the potential to enhance heat transfer for applications in industrial and manufacturing processes. Moreover, the term "nanofluid" was first established

---

* Corresponding author.
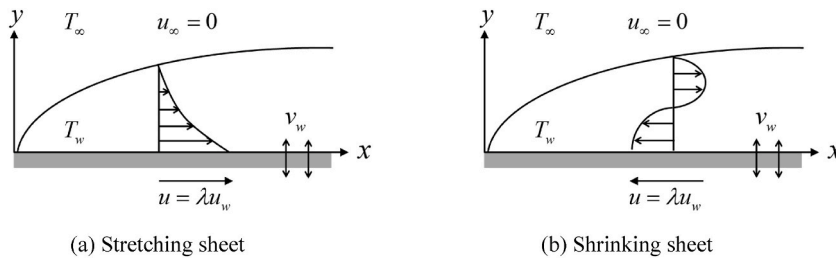*E-mail address:* iskandarwaini@utem.edu.my (I. Waini).

(a) Stretching sheet   (b) Shrinking sheet

Fig. 1. Flow configuration model.

Table 1
Thermophysical properties of hybrid nanofluid.

Thermophysical Properties	Hybrid nanofluid
Dynamic viscosity	$\mu_{hnf} = \dfrac{\mu_f}{(1-\varphi_{hnf})^{2.5}}$
Density	$\rho_{hnf} = (1-\varphi_{hnf})\rho_f + \varphi_1\rho_{n1} + \varphi_2\rho_{n2}$
Heat capacity	$(\rho C_p)_{hnf} = (1-\varphi_{hnf})(\rho C_p)_f + \varphi_1(\rho C_p)_{n1} + \varphi_2(\rho C_p)_{n2}$
Thermal conductivity	$\dfrac{k_{hnf}}{k_f} = \dfrac{\dfrac{\varphi_1 k_{n1} + \varphi_2 k_{n2}}{\varphi_{hnf}} + 2k_f + 2(\varphi_1 k_{n1} + \varphi_2 k_{n2}) - 2\varphi_{hnf}k_f}{\dfrac{\varphi_1 k_{n1} + \varphi_2 k_{n2}}{\varphi_{hnf}} + 2k_f - (\varphi_1 k_{n1} + \varphi_2 k_{n2}) + \varphi_{hnf}k_f}$

by Choi and Eastman [7]. In that study, they found that the addition of the nanoparticles in the base fluid enhanced the thermal conductivity. Further studies by Turcu et al. [8] as well as Jana et al. [10] showed that the thermal conductivity of the nanofluid may be further improved by additionally adding more than one nanoparticle type in the base fluid and this fluid, known as 'hybrid nanofluid'.

Takabi and Salehi [11] employed the use of hybrid nanofluid contained in a corrugated enclosure that comprising Al$_2$O$_3$–Cu nanoparticles and reported that the findings with respect to the experimental and modelling data are in good agreement with those of Suresh et al. [12]. The authors stated that heat transfer improvement occurred at higher concentrations of the nanoparticle volume fraction. Furthermore, Ghalambaz et al. [13] investigated the flow with respect to Al$_2$O$_3$–Cu/water hybrid nanofluid over a vertical plate. Here, the flow over a wedge was taken into consideration by Hassan et al. [14] and Mahanthesh et al. [15] in the presence of MoS$_2$–Ag as well as Cu–Ag hybrid nanoparticles, accordingly. Other studies on the hybrid nanofluids can be found in Refs. [16–19].

The flow and heat transfer of a hybrid nanofluid induced by a nonlinearly shrinking sheet in the presence of viscous dissipation has never been studied before, according to the literature already in existence. Concerning the research done by Cortell [5], a mathematical formulation of the current work is developed to close the knowledge gap mentioned above. In contrast to Cortell [5] research, ours takes into account a shrinking sheet having the hybrid nanoparticles (Al$_2$O$_3$–Cu) effect using the Takabi and Salehi [11] model. Furthermore, this research delves into the dual solutions and evaluates the temporal stability of the present problem. Additionally, it highlights the critical values of the physical parameter. These critical values are well-known for indicating the shift from laminar to turbulent boundary layer flow. Upon reaching this pivotal juncture, it opens up opportunities for strategically designing product processes to achieve desired results, ultimately boosting productivity.

2. Mathematical model

The Al$_2$O$_3$–Cu/water hybrid nanofluid flow induced by a non-linearly shrinking/stretching sheet is considered. The flow configuration model of the stretching and shrinking sheets are shown in Fig. 1 (a) and (b), respectively. Here, the surface velocity is $u_w(x)$ as well as the mass flux velocity is denoted by $v_w(x)$. Apart from that, the surface temperature is $T_w(x)$, while the constant ambient temperature is T_∞. The equations governing the hybrid nanofluid flow are given as follows (see Cortell [5,6]; Rohni et al. [9]):

$$\frac{\partial u}{\partial x} + \frac{\partial v}{\partial y} = 0 \tag{1}$$

$$u\frac{\partial u}{\partial x} + v\frac{\partial u}{\partial y} = \frac{\mu_{hnf}}{\rho_{hnf}}\frac{\partial^2 u}{\partial y^2} \tag{2}$$

$$u\frac{\partial T}{\partial x} + v\frac{\partial T}{\partial y} = \frac{k_{hnf}}{(\rho C_p)_{hnf}}\frac{\partial^2 T}{\partial y^2} + \frac{\mu_{hnf}}{(\rho C_p)_{hnf}}\left(\frac{\partial u}{\partial y}\right)^2 \tag{3}$$

subject to (see Cortell [5,6]; Rohni et al. [9]):

Table 2
Thermophysical properties of Al$_2$O$_3$, Cu, and water.

Thermophysical Properties	Al$_2$O$_3$	Cu	water
ρ (kg/m^3)	3970	8933	997.1
C_p (J/kgK)	765	385	4179
k (W/mK)	40	400	0.613
Prandtl number, Pr			6.2

$$v = v_w(x), u = u_w(x)\lambda, T = T_w(x) \quad \text{at} \quad y = 0$$

$$u \to 0, T \to T_\infty \quad \text{as} \quad y \to \infty \tag{4}$$

where u and v are respectively the velocity components along the x- and y- axes, while T represents the temperature. Meanwhile, the thermophysical correlations of hybrid nanofluid are provided in Table 1. It should be mentioned that the correlations in Table 1 were introduced by Takabi and Salehi [11], and also taken into consideration by numerous researchers, for instance, Ghalambaz et al. [13], Hassan et al. [14] and Mahanthesh et al. [15]. Table 2 provides the physical characteristics of Al$_2$O$_3$, Cu, as well as water (refer to Oztop and Abu-Nada [20]). Here, Al$_2$O$_3$ and Cu volume fractions are given by φ_1 and φ_2 where $\varphi_{hnf} = \varphi_1 + \varphi_2$, which the subscripts $n1$ as well as $n2$ are corresponding to their solid components, respectively. The fluid and the hybrid nanofluid are respectively identified by the subscripts f and hnf. Next, the surface velocity distribution is denoted in the power-law form, that is $u_w(x) = ax^n$, with $n = 1$ and $n \neq 1$ corresponds to the linear and nonlinear stretching/shrinking cases, respectively and the surface temperature is taken as $T_w(x) = T_\infty + T_0 x^{2n}$.

Following Cortell [5,6] and Rohni et al. [9], we define

$$u = ax^n f'(\eta), v = -\sqrt{\frac{a\nu_f(n+1)}{2}} x^{(n-1)/2} \left[f(\eta) + \frac{n-1}{n+1} \eta f'(\eta) \right]$$

$$\theta(\eta) = \frac{T - T_\infty}{T_w - T_\infty}, \eta = y\sqrt{\frac{a(n+1)}{2\nu_f}} x^{(n-1)/2} \tag{5}$$

On using (5), the transpiration rate at the surface is taken as (see Cortell [5,6]; Rohni et al. [9]):

$$v_w(x) = -\sqrt{\frac{a\nu_f(n+1)}{2}} x^{(n-1)/2} f(0) \tag{6}$$

where primes denote differentiation with respect to η. Eq. (1) is identically met, while Eq. (2) as well as (3) reduce to

$$\frac{\mu_{hnf}/\mu_f}{\rho_{hnf}/\rho_f} f''' + ff'' - \frac{2n}{n+1} f'^2 = 0 \tag{7}$$

$$\frac{1}{\text{Pr}} \frac{k_{hnf}/k_f}{(\rho C_p)_{hnf}/(\rho C_p)_f} \theta'' + f\theta' - \frac{4n}{n+1} f'\theta + \frac{\mu_{hnf}/\mu_f}{(\rho C_p)_{hnf}/(\rho C_p)_f} Ec f''^2 = 0 \tag{8}$$

Subject to:

$$f(0) = -S\sqrt{\frac{2}{n+1}}, f'(0) = \lambda, \theta(0) = 1$$

$$f'(\eta) \to 0, \theta(\eta) \to 0 \quad \text{as} \quad \eta \to \infty \tag{9}$$

where S denotes the mass suction/injection parameter with $S < 0$ for injection while $S > 0$ for suction, Pr resembles the Prandtl number and Ec denotes the Eckert number, defined as (see Cortell [5,6]; Rohni et al. [9]):

$$S = -\sqrt{\frac{n+1}{2}} f(0), \text{Pr} = \frac{(\mu C_p)_f}{k_f}, Ec = \frac{a^2}{(C_p)_f T_0} = \frac{u_w^2}{(C_p)_f (T_w - T_\infty)} \tag{10}$$

Note that $\lambda = -1$ and $\lambda = 1$ signify the shrinking as well as stretching sheets, while $\lambda = 0$ denotes the static sheet.

The skin friction coefficient C_f, as well as the local Nusselt number Nu_x are the physical quantities of interest for this problem, defined as (see Cortell [5,6]; Rohni et al. [9]):

$$C_f = \frac{\mu_{hnf}}{\rho_f u_w^2} \left(\frac{\partial u}{\partial y} \right)_{y=0}, Nu_x = -\frac{xk_{hnf}}{k_f (T_w - T_\infty)} \left(\frac{\partial T}{\partial y} \right)_{y=0} \tag{11}$$

Using (5 and 11), one gets:

$$
Re_x^{1/2} C_f = \frac{\mu_{hnf}}{\mu_f} \sqrt{\frac{n+1}{2}} f''(0), Re_x^{-1/2} Nu_x = -\frac{k_{hnf}}{k_f} \sqrt{\frac{n+1}{2}} \theta'(0) \tag{12}
$$

where $Re_x = u_w x / \nu_f$ represents the local Reynolds number.

3. Stability analysis

Results show that Eqs. (7)–(9) admit the dual solutions for several physical parameters. Consequently, further analysis is required to determine the stability of the solutions in the long run. To study the temporal stability of the solutions as time develops, we follow the works of Merkin [21] and Weidman et al. [22]. New variables are introduced relying on Eq. (5), and they are given as follows (see Waini et al. [23]):

$$
u = ax^n \frac{\partial f}{\partial \eta}(\eta, \tau), v = -\sqrt{\frac{a\nu_f(n+1)}{2}} x^{(n-1)/2} \left[f(\eta, \tau) + \frac{n-1}{n+1}\eta \frac{\partial f}{\partial \eta}(\eta, \tau) + 2\tau \frac{n-1}{n+1} \frac{\partial f}{\partial \tau}(\eta, \tau) \right]
$$

$$
\theta(\eta) = \frac{T - T_\infty}{T_w - T_\infty}, \eta = y\sqrt{\frac{a(n+1)}{2\nu_f}} x^{(n-1)/2}, \tau = atx^{n-1} \tag{13}
$$

Using (13), the unsteady form of Eqs. (1)–(3) are then transformed to

$$
\frac{\mu_{hnf}/\mu_f}{\rho_{hnf}/\rho_f} \frac{\partial^3 f}{\partial \eta^3} + f\frac{\partial^2 f}{\partial \eta^2} - \frac{2n}{n+1}\left(\frac{\partial f}{\partial \eta}\right)^2 - \frac{2}{n+1}\frac{\partial^2 f}{\partial \eta \partial \tau} - 2\tau\frac{n-1}{n+1}\left(\frac{\partial f}{\partial \eta}\frac{\partial^2 f}{\partial \eta \partial \tau} - \frac{\partial f}{\partial \tau}\frac{\partial^2 f}{\partial \eta^2}\right) = 0 \tag{14}
$$

$$
\frac{1}{Pr}\frac{k_{hnf}/k_f}{(\rho C_p)_{hnf}/(\rho C_p)_f}\frac{\partial^2 \theta}{\partial \eta^2} + f\frac{\partial \theta}{\partial \eta} - \frac{4n}{n+1}\frac{\partial f}{\partial \eta}\theta
$$

$$
+ \frac{\mu_{hnf}/\mu_f}{(\rho C_p)_{hnf}/(\rho C_p)_f} Ec\left(\frac{\partial^2 f}{\partial \eta^2}\right)^2 - \frac{2}{n+1}\frac{\partial \theta}{\partial \tau} - 2\tau\frac{n-1}{n+1}\left(\frac{\partial f}{\partial \eta}\frac{\partial \theta}{\partial \tau} - \frac{\partial f}{\partial \tau}\frac{\partial \theta}{\partial \eta}\right) = 0 \tag{15}
$$

Subject to:

$$
f(0,\tau) + 2\tau\frac{n-1}{n+1}\frac{\partial f}{\partial \tau}(0,\tau) = -S\sqrt{\frac{2}{n+1}}, \frac{\partial f}{\partial \eta}(0,\tau) = \lambda, \theta(0,\tau) = 1
$$

$$
\frac{\partial f}{\partial \eta}(\infty,\tau) = 0, \theta(\infty,\tau) = 0 \tag{16}
$$

Then, the disturbance is applied to the steady solution $f = f_0(\eta)$ as well as $\theta = \theta_0(\eta)$ of Eqs. (7)–(9) by employing the relations given by (refer to Weidman et al. [22]):

$$
f(\eta,\tau) = f_0(\eta) + e^{-\gamma\tau}F(\eta), \theta(\eta,\tau) = \theta_0(\eta) + e^{-\gamma\tau}G(\eta) \tag{17}
$$

in which $F(\eta)$ and $G(\eta)$ are smaller compared to $f_0(\eta)$ and $\theta_0(\eta)$. Moreover, the eigenvalue γ signs will identify the solutions' stability as time develops. By employing Eq. (17), and after linearization, Eqs. (14) and (15) become:

$$
\frac{\mu_{hnf}/\mu_f}{\rho_{hnf}/\rho_f}F''' + f_0 F'' + f_0'' F - \frac{4n}{n+1}f_0' F' + \frac{2}{n+1}\gamma F' = 0 \tag{18}
$$

$$
\frac{1}{Pr}\frac{k_{hnf}/k_f}{(\rho C_p)_{hnf}/(\rho C_p)_f}G'' + f_0 G' + \theta_0' F - \frac{4n}{n+1}\left(f_0' G + \theta_0 F'\right) + \frac{\mu_{hnf}/\mu_f}{(\rho C_p)_{hnf}/(\rho C_p)_f}2Ecf_0'' F'' + \frac{2}{n+1}\gamma G = 0 \tag{19}
$$

subject to:

$$
F(0) = 0, F'(0) = 0, G(0) = 0
$$

$$
F'(\infty) = 0, G(\infty) = 0 \tag{20}
$$

As per Harris et al. [24], without loss of generality, we fixed $F''(0) = 1$ to gain γ from Eq. (18) as well as (19).

Table 3

Values of $f''(0)$ with different values of S and n when $\lambda = 1$ (stretching sheet) for regular fluid ($\varphi_{hnf} = 0$).

S	n	Cortell [6]	Rohni et al. [9]	Present results
0	0.5	−0.88948	−0.889544	−0.889544
	0.75	−0.95379	−0.953957	−0.953957
	1.5	−1.06159	−1.061601	−1.061601
	7	−1.21685	−1.216852	−1.216850
	10	−1.23488	−1.234875	−1.234875
−1	0.5	−1.65026	−1.650420	−1.650420
	0.75	−1.63299	−1.633064	−1.633064
	1.5	−1.59316	−1.593215	−1.593215
	7	−1.47957	−1.479635	−1.479635
	10	−1.45446	−1.454544	−1.454544

4. Results and discussion

MATLAB software is employed to code Eqs. (7)–(9). The detailed procedures are described by Shampine et al. [25]. In this study, the total composition of Al_2O_3 and Cu volume fractions are implemented in a one-to-one ratio. For example, 1% of Al_2O_3 ($\varphi_1 = 1\%$) as well as 1% of Cu ($\varphi_2 = 1\%$) are mixed to form 2% of Al_2O_3–Cu hybrid nanoparticles volume fractions, known as $\varphi_{hnf} = 2\%$.

The numerical procedures can be outlined as follows: Initially, we convert Eqs. (7) and (8) into a set of first-order ordinary differential equations. Thus, Eq. (7) can be written as:

$$f = y(1),$$

$$f' = y'(1) = y(2), \tag{21a}$$

$$f'' = y'(2) = y(3), \tag{21b}$$

$$f''' = y'(3) = -\frac{\rho_{hnf}/\rho_f}{\mu_{hnf}/\mu_f}\left(y(1)y(3) - \frac{2n}{n+1}y(2)^2\right), \tag{21c}$$

while Eq. (8) reduces to:

$$\theta = y(4),$$

$$\theta' = y'(4) = y(5), \tag{22a}$$

$$\theta'' = y'(5) = -\mathrm{Pr}\frac{(\rho C_p)_{hnf}/(\rho C_p)_f}{k_{hnf}/k_f}\left(y(1)y(5) - \frac{4n}{n+1}y(2)y(4) + \frac{\mu_{hnf}/\mu_f}{(\rho C_p)_{hnf}/(\rho C_p)_f}Ecy(3)^2\right), \tag{22b}$$

and the boundary condition (9) becomes:

$$y_a(1) = = -S\sqrt{\frac{2}{n+1}}, y_a(2) = \lambda, y_a(4) = 1,$$

$$y_b(2) \longrightarrow 0, y_b(4) \longrightarrow 0. \tag{23}$$

The subscript 'a' signifies the surface condition, whereas 'b' represents the free stream condition. Following this, we apply Eqs. (21)–(23) within the Matlab software and utilize the bvp4c solver for solving them. The solver will then proceed to generate numerical solutions and graphical representations.

Additionally, the critical values of the physical parameters have also been determined. Essentially, we have two codes (referred to as code A and code B) for generating the critical values. Here is a brief explanation of how to calculate the critical values:

For instance, in code A, a value for the power law index parameter, n is set, let's say $n = 1.5$. Then, a new value of n with a small variation (for example, within one decimal place) is considered in code B. Subsequently, a numerical solution based on this new value of n is obtained using code B. The critical value is determined when the first and second solutions merge. These steps are repeated, considering values of n up to four decimal places, until reaching the critical value of the desired power law index parameter n and numerical computations beyond this critical value become impossible. From our calculation, the critical value of n for fixed values of $S = -2.5$, $Ec = 0.1$, $\mathrm{Pr} = 6.2$, $\lambda = -1$, and $\varphi_{hnf} = 2\%$ is $n_c = 2.0104$.

To ensure the accuracy of the calculations, we validate our current results by comparing them to the data published in previous studies. Table 3 compares the values of $f''(0)$ with those of Cortell [6] and Rohni et al. [9] for distinct S and n values provided that $\lambda = 1$

Table 4
Values of $-\theta'(0)$ with different Ec and n when $Pr = 5, S = 0$ and $\lambda = 1$ (stretching sheet) for regular fluid ($\varphi_{hnf} = 0$).

Ec	n	Cortell [5]	Present results
0	0.5		2.852380
	0.75	3.124975	3.125340
	1.5	3.567737	3.567962
	7	4.185373	4.185469
	10	4.255972	4.255984
0.1	0.5		2.745400
	0.75	3.016983	3.017033
	1.5	3.455721	3.455914
	7	4.065722	4.065792
	10	4.135296	4.135302

Table 5
Values of $Re_x^{1/2} C_f$ and $Re_x^{-1/2} Nu_x$ with different values of physical parameters when $Pr = 6.2$ and $\lambda = -1$ (shrinking sheet) for Al_2O_3–Cu/water ($\varphi_{hnf} = 2\%$).

n	S	Ec	$Re_x^{1/2} C_f$		$Re_x^{-1/2} Nu_x$	
			First solution	Second solution	First solution	Second solution
1	−2	0	1.362196 (1.3622)	0.856614 (0.8566)	10.660376	10.540562
1	−2.5	0.1	2.256364	0.517144	13.379079	12.902573
1.5			1.970060	0.594669	12.744586	11.991199
2			1.366558	1.166694	11.812654	11.674552
2	−2.6		1.768833	0.836636	12.709052	12.075533
	−2.8		2.196414	0.529475	14.190416	13.030090
	−3		2.535564	0.269391	15.571065	13.869699
	−3	0.2	2.535564	0.269391	14.526164	11.478421
		0.3	2.535564	0.269391	13.481264	9.087143
		0.4	2.535564	0.269391	12.436364	6.695864

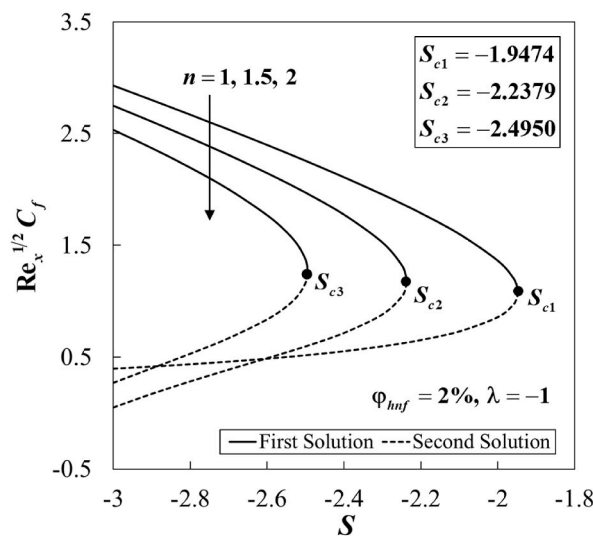Note: Results in ( ) are from Waini et al. [23].

Fig. 2. Plot of $Re_x^{1/2}C_f$ against λ for various n.

(stretching sheet) and $\varphi_{hnf} = 0$ (regular fluid). It shows a good agreement between those results. On the other hand, Table 4 illustrates the comparison values with respect to $-\theta'(0)$ with Cortell [5] for different Ec and n when $Pr = 5, S = 0, \lambda = 1$ (stretching sheet) as well as $\varphi_{hnf} = 0$ (regular fluid). We notice that the comparison is satisfactory with the literature review that has been mentioned earlier. Moreover, Table 5 illustrates the values with respect to $Re_x^{1/2} C_f$ and $Re_x^{-1/2} Nu_x$ with distinct values of physical parameters provided that $Pr = 6.2$ and $\lambda = -1$ (shrinking sheet) for Al_2O_3–Cu/water ($\varphi_{hnf} = 2\%$). The rising of power-law index n (from $n = 1$ to $n = 2$)
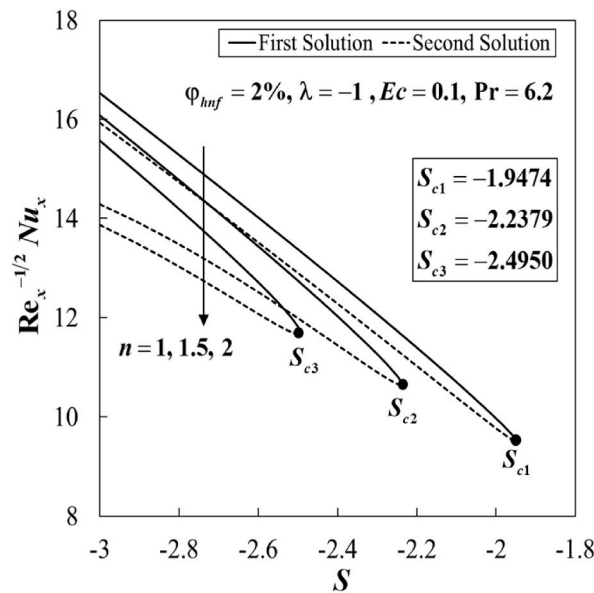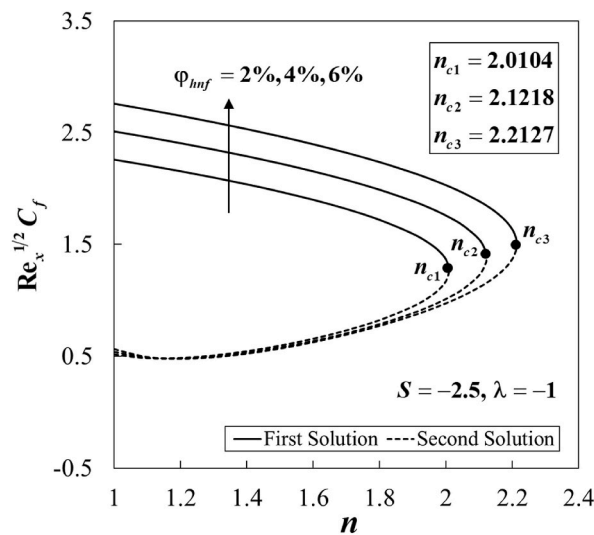
Fig. 3. Plot of $Re_x^{-1/2} Nu_x$ against λ for various n.

Fig. 4. Plot of $Re_x^{1/2} C_f$ against λ for various φ_{hnf}.

leads to a decrease in the values of $Re_x^{1/2} C_f$ and $Re_x^{-1/2} Nu_x$ for the first solutions with 39.44 % and 11.71 % reduction, respectively. Meanwhile, the values of these physical quantities are increased for stronger suction strength $(S < 0)$. Moreover, the effect of larger Eckert number Ec (from $Ec = 0.2$ to $Ec = 0.4$) is to decrease the heat transfer rate, $Re_x^{-1/2} Nu_x$ with 14.39 % reduction. Additionally, the comparison of $Re_x^{1/2} C_f$ for Al$_2$O$_3$–Cu/water with Waini et al. [23] also show an excellent agreement.

Figs. 2 and 3 show the variations with respect to $Re_x^{1/2} C_f$ as well as $Re_x^{-1/2} Nu_x$ against S with a variety of values of n for Al$_2$O$_3$–Cu/water $(\varphi_{hnf} = 2\%)$ when $Ec = 0.1$, $\mathrm{Pr} = 6.2$, as well as $\lambda = -1$ (shrinking sheet). These figures show that the $Re_x^{-1/2} Nu_x$ and $Re_x^{1/2} C_f$ values are reduced for bigger values of S and n. Conversely, when the selected parameters are held constant, we observe that dual solutions become accessible within a specific range of suction strength S with critical points occurring at $S_c = -1.9474, -2.2379, -2.4950$ for $n = 1, 1.5, 2$, respectively. The discovery is in accordance with the idea put out by Miklavčič and Wang [3] that the only way to force a flow across a surface that is shrinking is to apply an adequate suction strength to it. Also, these figures reveal that the boundary layer separates faster for bigger values of n.

In addition, the variations of $Re_x^{1/2} C_f$ as well as $Re_x^{-1/2} Nu_x$ against n for several compositions of φ_{hnf} provided that $S = -2.5$, $Ec = 0.1$, $\mathrm{Pr} = 6.2$, as well as $\lambda = -1$ (shrinking sheet) are demonstrated in Figs. 4 and 5. Results show that the higher composition of hybrid
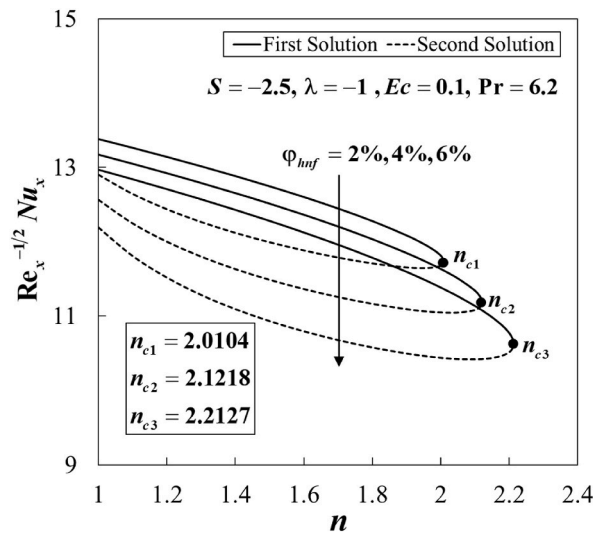
Fig. 5. Plot of $Re_x^{-1/2}Nu_x$ against λ for various φ_{hnf}.
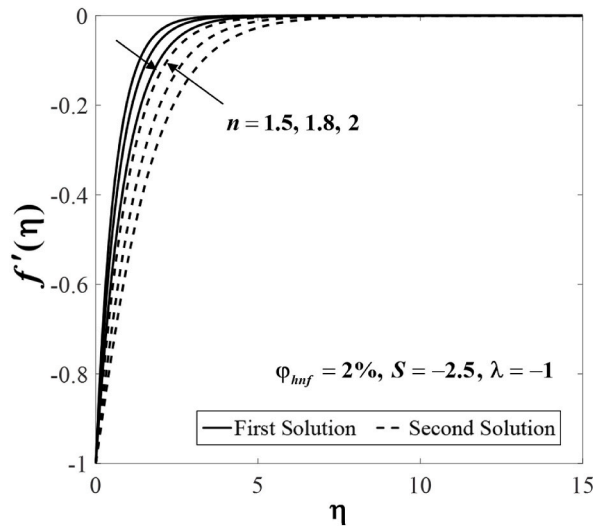

Fig. 6. Impact of n on $f'(\eta)$.

nanoparticles leads to enhance the values of $Re_x^{1/2}C_f$ but reduce the values of $Re_x^{-1/2}Nu_x$. This is in contrast with that of the stretching counterpart, where both of the local Nusselt number and the skin friction coefficient increase with higher composition of the hybrid nanoparticles. It is interesting to observe that the dual solutions live for some values of n where the critical values occur at $n_c = 2.0104$, $2.1218, 2.2127$ for $\varphi_{hnf} = 2\%, 4\%, 6\%$, respectively. This observation reveals that, for fixed values of the selected parameters, the variations of the power-law index n of the surface velocity cannot exceed the critical values n_c.

Further, Figs. 6 and 7 portray the effect of the power-law index, n on $f'(\eta)$ as well as $\theta(\eta)$ when $S = -2.5, \lambda = -1, Ec = 0.1, \Pr = 6.2$ and $\varphi_{hnf} = 2\%$. Note that the profiles of $f'(\eta)$ is decreased and $\theta(\eta)$ is increased with larger n (see results for the first solution). Physically, when $n = 1$, the velocity profile follows a linear distribution. Meanwhile, when $n > 1$, the velocity profile exhibits an accelerating trend where the velocity increases, resulting in a steeper velocity gradient. Consequently, the fluid temperature is enhanced with the rise of n. However, the behavior is opposite in the shrinking sheet case where the fluid velocity is decreasing and leads to the reduction in the velocity gradient. Besides, it is noticed that the profiles of the first and the second solutions combine to some values of n. This observation agrees with the outcomes obtained in Figs. 4 and 5.

Besides, the profiles of $f'(\eta)$ and $\theta(\eta)$ when $n = 2, S = -2.5, \lambda = -1, Ec = 0.1$, and $\Pr = 6.2$ for several compositions of φ_{hnf} are displayed in Figs. 8 and 9. It is clear that both branch solutions of $\theta(\eta)$ depict an improving pattern for higher compositions of φ_{hnf}. Meanwhile, the profiles of $f'(\eta)$ increases for the first solution but drops for the second solution. These characteristics are impacted by
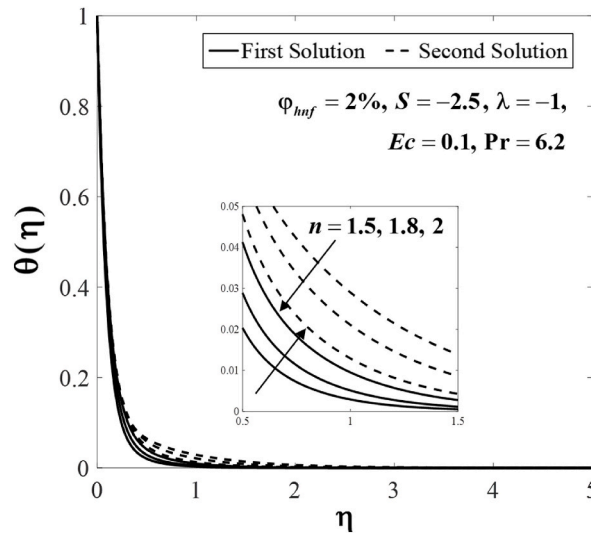
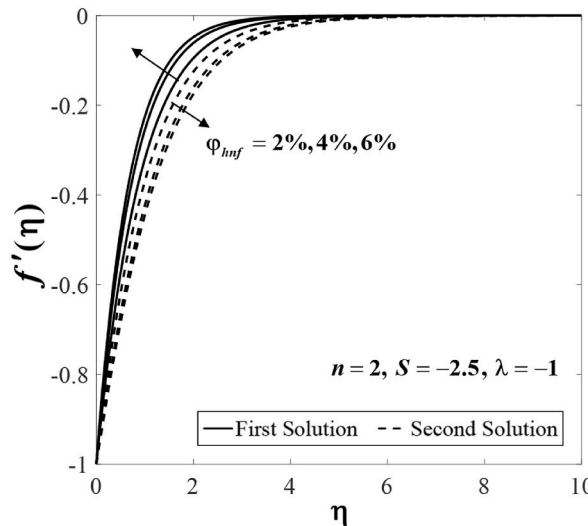**Fig. 7.** Impact of n on $\theta(\eta)$.

Fig. 8. Impact of φ_{hnf} on $f'(\eta)$.

the incorporation of nanoparticles, which elevate the fluid's viscosity, resulting in deceleration and reduced flow velocity. Additionally, nanoparticles contribute to energy dissipation in the form of heat, leading to elevated temperatures.

Next, the effect of Ec on $\theta(\eta)$ when $n = 2, S = -2.5, \lambda = -1, \Pr = 6.2,$ and $\varphi_{hnf} = 2\%$ is illustrated in Fig. 10. An increasing pattern on both branch solutions with regard to $\theta(\eta)$ is observed for greater values of Ec. Physically, the Eckert number represents the ratio of kinetic energy flow to the boundary layer's enthalpy difference. It facilitates the conversion of kinetic energy into internal energy by counteracting fluid stresses. This leads to a decrease in the effect of enthalpy difference due to the dominant kinetic energy. Consequently, the thermal layer thickness increases, resulting in a rise in fluid temperature.

The variations of γ against n provided that $S = -2.5, \lambda = -1,$ while $\varphi_{hnf} = 2\%$ are demonstrated in Fig. 11. This figure depicts that the sign of γ is positive for the first solution but negative for the second solution. Referring to Eq. (17), $e^{-\gamma\tau} \to 0$ as $\tau \to \infty$ for $\gamma > 0$ and $e^{-\gamma\tau} \to \infty$ for $\gamma < 0$. This outcome suggests that, over time, the first solution remains stable, whereas the second solution displays instability and is therefore not suitable for long-term physical representation.

5. Conclusion

In the current study, the problem of hybrid nanofluid flow over a non-linearly shrinking sheet was achieved. The influences of multiple physical parameters on the flow behavior were investigated. Findings that dual solutions are disclosed for a particular range
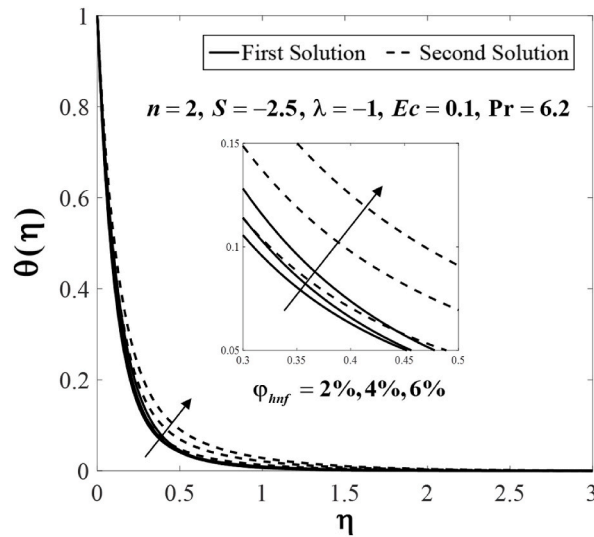
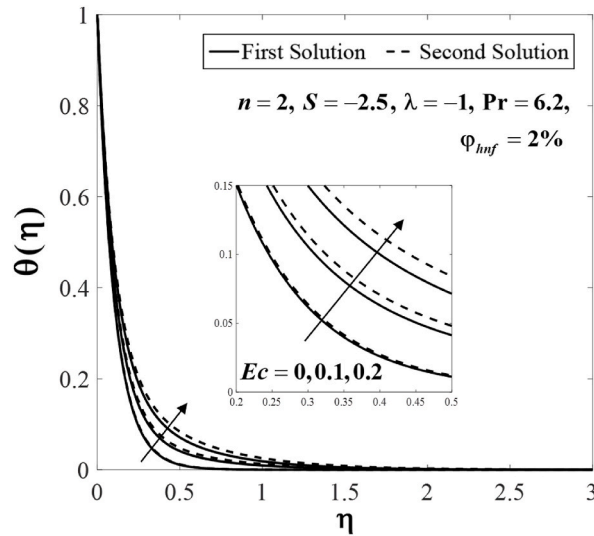**Fig. 9.** Impact of φ_{hnf} on $\theta(\eta)$.

Fig. 10. Impact of Ec on $\theta(\eta)$.

of the mass flux parameter S as well as the power-law index n. The rise of the power-law index n led to reduce the skin friction co-efficient as well as heat transfer rate with 39.44 % and 11.71 % reduction, respectively. The larger Ec (from $Ec = 0.2$ to $Ec = 0.4$) contributed to reducing the heat transfer rate with 14.39 % reduction. It was found that the first solution is stable as time evolves. For the stable solution, higher composition of hybrid nanoparticles led to enhance the skin friction coefficient but reduce the local Nusselt number. As future recommendations, this study can be extended to different geometries such as wedge and cylinder surfaces. Also, the effects of several temperature conditions such as Newtonian heating, and convective boundary condition can be considered. Moreover, hybrid nanofluid cooperated with non-Newtonian fluid models also can be examined, for example, Eyring-Powell, and Reiner-Phillipoff fluids.

Data availability statement

Data will be made available on request.

Additional information

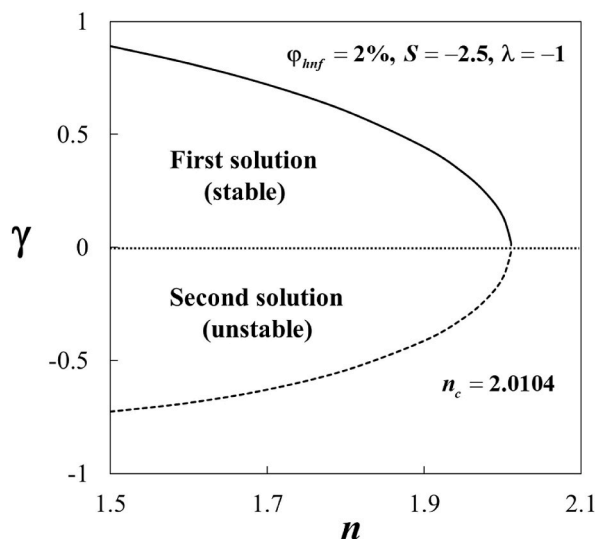No additional information is available for this paper.

Fig. 11. Plot of γ against n.

CRediT authorship contribution statement

Iskandar Waini: Validation, Visualization, Writing – original draft. **Sumayyah Alabdulhady:** Validation, Writing – original draft. **Anuar Ishak:** Conceptualization, Supervision, Writing – review & editing. **Ioan Pop:** Conceptualization, Supervision, Writing – review & editing.

Declaration of competing interest

The authors declare that they have no known competing financial interests or personal relationships that could have appeared to influence the work reported in this paper.

Acknowledgements

References

[1] L.J. Crane, Flow past a stretching plate, Zeitschrift Für Angewandte Mathematik Und Physik ZAMP. 21 (1970) 645–647, https://doi.org/10.1007/BF01587695.
[2] S. Goldstein, On backward boundary layers and flow in converging passages, J. Fluid Mech. 21 (1965) 33–45, https://doi.org/10.1017/S0022112065000034.
[3] M. Miklavčič, C.Y. Wang, Viscous flow due to a shrinking sheet, Q. Appl. Math. 64 (2006) 283–290, https://doi.org/10.1090/S0033-569X-06-01002-5.
[4] K. Vajravelu, Viscous flow over a nonlinearly stretching sheet, Appl. Math. Comput. 124 (2001) 281–288, https://doi.org/10.1016/S0096-3003(00)00062-X.
[5] R. Cortell, Viscous flow and heat transfer over a nonlinearly stretching sheet, Appl. Math. Comput. 184 (2007) 864–873, https://doi.org/10.1016/j.amc.2006.06.077.
[6] R. Cortell, Combined effect of viscous dissipation and thermal radiation on fluid flows over a non-linearly stretched permeable wall, Meccanica 47 (2012) 769–781, https://doi.org/10.1007/s11012-011-9488-z.
[7] S.U.S. Choi, J.A. Eastman, Enhancing thermal conductivity of fluids with nanoparticles, in: Proceedings of the 1995 ASME International Mechanical Engineering Congress and Exposition, FED 231/MD, vol. 66, 1995, pp. 99–105, https://doi.org/10.1115/1.1532008.
[8] R. Turcu, A. Darabont, A. Nan, N. Aldea, D. Macovei, D. Bica, L. Vekas, O. Pana, M.L. Soran, A.A. Koos, L.P. Biro, New polypyrrole-multiwall carbon nanotubes hybrid materials, J. Optoelectron. Adv. Mater. 8 (2006) 643–647.
[9] A.M. Rohni, S. Ahmad, I. Pop, Note on Cortell's non-linearly stretching permeable sheet, Int. J. Heat Mass Tran. 55 (2012) 5846–5852, https://doi.org/10.1016/j.ijheatmasstransfer.2012.05.080.
[10] S. Jana, A. Salehi-Khojin, W.H. Zhong, Enhancement of fluid thermal conductivity by the addition of single and hybrid nano-additives, Thermochim. Acta 462 (2007) 45–55, https://doi.org/10.1016/j.tca.2007.06.009.
[11] B. Takabi, S. Salehi, Augmentation of the heat transfer performance of a sinusoidal corrugated enclosure by employing hybrid nanofluid, Adv. Mech. Eng. 6 (2014), 147059, https://doi.org/10.1155/2014/147059.
[12] S. Suresh, K.P. Venkitaraj, P. Selvakumar, M. Chandrasekar, Synthesis of Al2O3-Cu/water hybrid nanofluids using two step method and its thermo physical properties, Colloids Surf. A Physicochem. Eng. Asp. 388 (2011) 41–48, https://doi.org/10.1016/j.colsurfa.2011.08.005.
[13] M. Ghalambaz, N.C. Rosca, A. v Rosca, I. Pop, Mixed convection and stability analysis of stagnation-point boundary layer flow and heat transfer of hybrid nanofluids over a vertical plate, Int. J. Numer. Methods Heat Fluid Flow 30 (2020) 3737–3754, https://doi.org/10.1108/HFF-08-2019-0661.
[14] M. Hassan, A. Faisal, I. Ali, M.M. Bhatti, M. Yousaf, Effects of Cu–Ag hybrid nanoparticles on the momentum and thermal boundary layer flow over the wedge, Proc. IME E J. Process Mech. Eng. 233 (2019) 1128–1136, https://doi.org/10.1177/0954408919844668.
[15] B. Mahanthesh, S.A. Shehzad, T. Ambreen, S.U. Khan, Significance of Joule heating and viscous heating on heat transport of MoS2–Ag hybrid nanofluid past an isothermal wedge, J. Therm. Anal. Calorim. 143 (2021) 1221–1229, https://doi.org/10.1007/s10973-020-09578-y.

[16] I. Waini, A. Ishak, I. Pop, Melting heat transfer of a hybrid nanofluid flow towards a stagnation point region with second-order slip, Proc. IME E J. Process Mech. Eng. 235 (2021) 405–415, https://doi.org/10.1177/0954408920961213.

[17] I. Waini, A. Ishak, I. Pop, Unsteady hybrid nanofluid flow on a stagnation point of a permeable rigid surface, ZAMM Zeitschrift Fur Angewandte Mathematik Und Mechanik 101 (2021), e202000193, https://doi.org/10.1002/zamm.202000193.

[18] I. Waini, A. Ishak, I. Pop, Radiative and magnetohydrodynamic micropolar hybrid nanofluid flow over a shrinking sheet with Joule heating and viscous dissipation effects, Neural Comput. Appl. (2021), https://doi.org/10.1007/s00521-021-06640-0, 10.1007/s00521-021-06640-0.

[19] I. Waini, U. Khan, A. Zaib, A. Ishak, I. Pop, Thermophoresis particle deposition of CoFe2O4-TiO2 hybrid nanoparticles on micropolar flow through a moving flat plate with viscous dissipation effects, Int. J. Numer. Methods Heat Fluid Flow (2022), https://doi.org/10.1108/HFF-12-2021-0767.

[20] H.F. Oztop, E. Abu-Nada, Numerical study of natural convection in partially heated rectangular enclosures filled with nanofluids, Int. J. Heat Fluid Flow 29 (2008) 1326–1336, https://doi.org/10.1016/j.ijheatfluidflow.2008.04.009.

[21] J.H. Merkin, On dual solutions occurring in mixed convection in a porous medium, J. Eng. Math. 20 (1986) 171–179, https://doi.org/10.1007/BF00042775.

[22] P.D. Weidman, D.G. Kubitschek, A.M.J. Davis, The effect of transpiration on self-similar boundary layer flow over moving surfaces, Int. J. Eng. Sci. 44 (2006) 730–737, https://doi.org/10.1016/j.ijengsci.2006.04.005.

[23] I. Waini, A. Ishak, I. Pop, Hybrid nanofluid flow over a permeable non-isothermal shrinking surface, Mathematics 9 (2021) 538, https://doi.org/10.3390/math90505.

[24] S.D. Harris, D.B. Ingham, I. Pop, Mixed convection boundary-layer flow near the stagnation point on a vertical surface in a porous medium: brinkman model with slip, Transport Porous Media 77 (2009) 267–285, https://doi.org/10.1007/s11242-008-9309-6.

[25] L.F. Shampine, I. Gladwell, S. Thompson, Solving ODEs with MATLAB, Cambridge University Press, Cambridge, 2003, https://doi.org/10.1017/cbo9780511615542.

Nomenclature

a: constant
C_f: skin friction coefficient
C_p: specific heat at constant pressure $(Jkg^{-1}K^{-1})$
(ρC_p): heat capacitance of the fluid $(JK^{-1}m^{-3})$
Ec: Eckert number
$f(\eta)$: dimensionless stream function
n: power law index
k: thermal conductivity of the fluid $(Wm^{-1}K^{-1})$
Nu_x: local Nusselt number
Pr: Prandtl number
Re_x: local Reynolds number
S: mass flux parameter
t: time (s)
T: fluid temperature (K)
T_w: surface temperature (K)
u,v: velocity component in the x- and y-directions (ms^{-1})
u_w: surface velocity (ms^{-1})
v_w: mass flux velocity (ms^{-1})
x,y: Cartesian coordinates (m)

Greek symbols

γ: eigenvalue
η: similarity variable
θ: dimensionless temperature
λ: stretching/shrinking parameter
μ: dynamic viscosity of the fluid $(kgm^{-1}s^{-1})$
ν: kinematic viscosity of the fluid (m^2s^{-1})
ρ: density of the fluid (kgm^{-3})
τ: dimensionless time variable
φ_1: nanoparticle volume fractions for Al_2O_3 (alumina)
φ_2: nanoparticle volume fractions for Cu (copper)
ψ: stream function

Subscripts

f: base fluid
nf: nanofluid
hnf: hybrid nanofluid
$n1$: solid component for Al_2O_3 (alumina)
$n2$: solid component for Cu (copper)

Superscript

$'$: differentiation with respect to η